5-2019

Exclusive neutral pion production and Compton scattering at GlueX

Zach Baldwin

Exclusive π^0 production and Compton scattering at GlueX

A thesis submitted in partial fulfillment of the requirement for the degree of Bachelor of Science with Honors in Physics from The College of William and Mary in Virginia,

by

Zachary A. Baldwin

Accepted for Honors
(Honors or no-Honors)

Advisor: Prof. Justin Stevens, Physics

Prof. Seth Aubin, Physics

Prof. Margaret Saha, Biology

Department of Physics
College of William and Mary
Williamsburg, Virginia
May 1st, 2019

Abstract

By using data collected from Thomas Jefferson National Accelerator (JLab), I will be observing two specific reactions from the collision of linearly polarized photons with protons in a liquid hydrogen target. In this work, studies of the reaction $\gamma p \to \pi^0 p$ will be presented along with an exploratory study of the Compton scattering process $\gamma p \to \gamma p$. These reactions were studied by utilizing the fine-grained calorimetry of the GlueX experiment in order to aid in the understanding of meson production mechanisms in high-energy photoproduction. The separation of π^0 and Compton events is challenging due to potential merging of the π^0 decay photons into a single shower for large polar angles and high momentum. This merging causes π^0 decay photons with a small opening angle to look like single Compton photon showers. As a result, electromagnetic shower shape variables are used to study these effects, and with the introduction of three new width variables, comparisons between data and Monte Carlo samples are obtained to estimate the signal purity for these two reactions. These results will provide a stepping stone to ultimately measure the Σ beam asymmetry for large angle Compton scattering events.

Contents

Chapter 1

Introduction

The GlueX experiment at Jefferson Lab's Hall D aims to explore the gluonic degrees of freedom within hadrons through high-energy meson photoproduction. In high-energy photoproduction, the dominant meson exchange is theorized to be due to the exchange of massive quasi-particles called Reggeons. Understanding this type of meson exchange is vital in order to search for gluonic excitations in the meson spectrum through photoproduction reactions.

To understand how this massive quasi-particle exchange works then, an approach to observing the theorized quantum numbers for the leading trajectories of the vector and axial-vector Reggeons needs to occur. These quantum numbers are gathered by measuring the linearly polarized photon beam asymmetry.

Along with observing the high-energy Reggeon exchange, the exploratory study of the Compton scattering process may provide the potential for constraining Generalized Parton Distributions (GPDs) of the proton. These GPDs describe the transverse position and longitudinal momentum of quarks in the proton.

Using a 9 GeV linearly polarized photon beam, first measurements of the Σ beam asymmetry (described in detail in Chapter 2.2) for pseudo-scalar production have already provided insight into the meson production mechanisms at these high-energies. Calculations taken previously at the Stanford Linear Accelerator Center show a sig-

nificant dip in asymmetries at around $-t = 0.5(GeV/c)^2$ for $\gamma p \to \pi^0 p$, while more recent π^0 measurements at GlueX show no dip [1]. Without this dip, then it is theorized that there is a strong influence of the vector Reggeon exchange around this energy. Through this honors project, I will hopefully enhance this endeavour by exploiting new moment variables and using the newest experimental data (with considerably better statistics than before) to observe both $\gamma p \to \gamma \pi^0$ and $\gamma p \to \gamma p$ reactions. With over a year's work being completed through depletion of background data and separating the two particle reactions, much progress has been made, but it is apparent that there is still a significant amount of work to be done.

This Honors thesis report is laid out in the following order: Theory (Chapter 2), Experimental Setup (Chapter 3), Results (Chapter 4), Conclusion (Chapter 5), References (Chapter 6).

Chapter 2

Theory

To understand this research, then a broad understanding of several topics are needed including but not limited to: lattice quantum chromodynamics (lattice QCD), linearly polarized photon beam asymmetries, and Monte Carlo (MC) simulations.

2.1 Meson production

Mesons are described as subatomic particles composed of one quark and one anti-quark. For the purposes of this thesis, there is a need to look at spectroscopy within a specific model called the constituent quark model. In this model, the quark and anti-quark pair are bound together by the strong interaction and are usually represented as, $q\overline{q}$.

Developed by Murray Gell-Mann, the Eightfold way organizes hadrons (in our case mesons) accurately, as depicted in Fig. 2.1 [7].

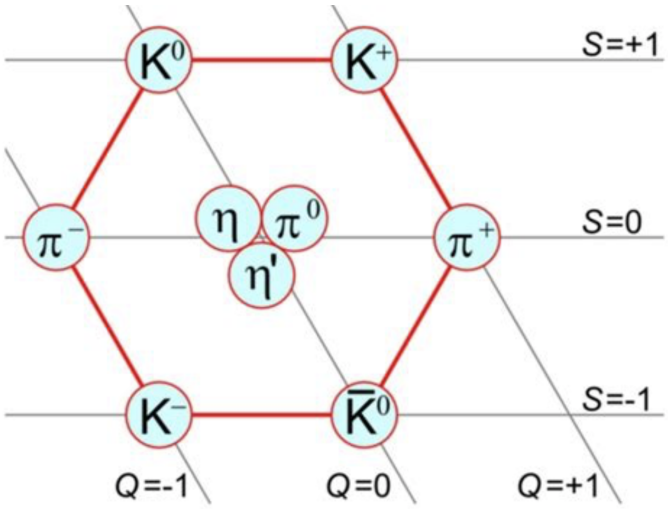

Figure 2.1: This is the meson nonet as described in Gell-Man's eight-fold way of organizing hadrons. The mesons increase in strangeness as you go up the diagram and increase in charge as you go from left to right.

This diagram in Fig. 2.1 shows the 9 pseudoscalar mesons (a meson with total spin 0 with odd parity) arranged by strangeness (S= +1,0,-1) and electric charge (Q= -1, 0, +1). Here, strangeness is defined by

$$S = -(n_s + n_{\bar{s}}), \tag{2.1}$$

where n_s is the number of strange quarks and $n_{\bar{s}}$ is the number of strange anti-quarks. While the electric charge is gathered from the total number of up quarks (Q=+2/3) and down quarks (Q=-1/3) in the meson.

Mesons can also be described by another property known as the isospin which is calculated as

$$I_3 = \frac{(n_u - n_d)}{2}, \tag{2.2}$$

where n_u and n_d are the number of up and down quarks, respectively. This isospin is what helps differ some mesons apart when they have the same masses. For example, the three pions were thought to be the same particle when first discovered, but their isospin was what made each of them different [8].

2.1.1 Lattice Quantum Chromodynamics

Lattice QCD is a well established non-perturbative approach to solving quantum chromodynamics, which is the theory of gluons and quarks. It is a lattice gauge theory formulated on a grid or lattice of points in space and time that studies the strong interactions of quarks and gluonic fields. The reason that this research focuses on lattice QCD is because strong interactions are

(1) Confining

(2) Chirally broken (in regards to chiral symmetry)

The confining portion just means that the strong interaction holds most ordinary matter together since it "confines" quarks into hadrons (*e.g* neutrons and protons). This confinement is known as non-perturbative which means that all the results can not be calculated numerically through perturbation theory to arbitrary accuracy on a computer.

The chirally broken portion just means that the particles are not symmetric. Essentially, we can define the particle's spin as something called handedness. When the particle is massless, as in a photon, then this handedness is the exact same as chirality. There can be a symmetry transformation between two particles which can be called parity. So, invariance (*i.e.* remaining unchanged) under parity transformation by a fermion is known as chiral symmetry. In most theories for QCD, this chiral symmetry can be broken, thus making it non-perturbative.

Since lattice QCD is the only approach to hadronic physics that is able to handle non-perturbative properties from the first principles of quark and gluon interations, it is a key method for understanding the strong nuclear force.

2.1.2 Quantum Numbers

In the strong interaction, there are several conserved quantities. Some of the quantities are listed below:

- Electric Charge (**Q**)
- Parity (**P**)
- Isospin (**I**)
- Angular Momentum (**J**)
- Strangeness (**S**)
- G-Parity (**G**)
- Charge conjugation (**C**)

In Table 1 below, we can see that some of these conserved quantities are carried by quarks.

Quark	**Q**	**J**	**S**	**I**
u	2/3	1/3	0	1/2
d	-1/3	1/2	0	1/2
s	-1/3	1/2	-1	0

Table 1: Quantum numbers of the three lightest quarks. [3]

From the constituent quark model, there can be a total angular momentum denoted as **J**. The total angular momentum can be calculated by

$$\mathbf{J} = \mathbf{L} \oplus \mathbf{S} \tag{2.3}$$

where the orbital angular momentum is denoted by **L**, and the total spin of the quarks is denoted by **S** (the total spin would be either 0 or 1 for the $q\overline{q}$ pair).

The total angular momentum **J** must take on the following values:

$$\mathbf{J} = |\mathbf{L} - \mathbf{S}|, |\mathbf{L} - \mathbf{S} + 1|, ..., |\mathbf{L} + \mathbf{S}| \tag{2.4}$$

.

From these quantities then the $\mathbf{J^{PC}}$ quantum numbers of any meson can be calculated.

The first model developed for high-energy $\gamma p \rightarrow \pi^0 p$ by Goldstein and Owens was based on the exchange of Reggeons with the allowed t-channel quantum numbers $\mathbf{J^{PC}} = 1^{--}$ and 1^{+-} [1]. This model is described in more context in section 2.1.3. This model is the representation that will be used when the $\mathbf{J^{PC}}$ numbers are extracted for π^0 production. There is currently no model that supports the $\mathbf{J^{PC}}$ numbers for Compton scattering processes so this project will be the first to look for these values.

2.1.3 Mandelstam variables

From theory, Mandelstam variables are numerical quantities that use the energy, momentum, and angles of particles in a hadronic scattering process. There are three variables: t-channel (time channel), s-channel (space channel), and u-channel.

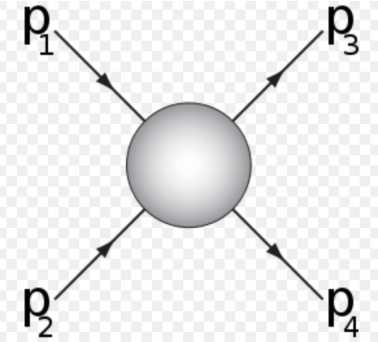

Figure 2.2: This is a Feynman diagram of a simple hadronic interaction. Here, p_1, p_2, p_3, p_4 are all particles. According to theory, there are specific ways in which the initial states react and produce specific final states.

The variables are defined using the Feynman diagram shown above in Fig. 2.2.

$$s = (p_1 + p_2)^2 = (p_3 + p_4)^2 \tag{2.5}$$

$$t = (p_1 - p_3)^2 = (p_4 - p_2)^2 \tag{2.6}$$

$$u = (p_1 - p_4)^2 = (p_3 - p_2)^2 \tag{2.7}$$

Each channel represents a different scattering process. The only channel this project observes is the time channel shown in Fig. 2.3 below.

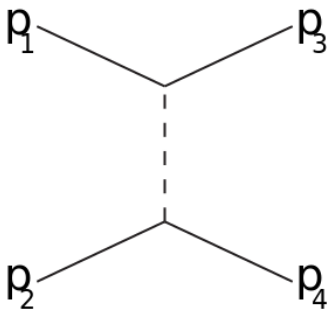

Figure 2.3: This is a example Feynmann diagram for a T-channel interaction. For a reference for my specific reactions, p_1 is the incoming γ photon , p_2 is the incoming proton, p_3 is the π^0 or the produced γ photon, and p_4 is the same proton as p_2 but with less momentum as before.

This diagram represents the process where particle 1 emits the intermediate particle and becomes the final particle 3, while particle 2 absorbs the intermediate particle and becomes particle 4.

2.1.4 Reactions

For this research, I will be looking at two distinct reactions. These are $\gamma p \to \gamma p$ and $\gamma p \to \pi^0 p$. What these specifically mean is that by using Jefferson Lab's accelerator, I will be studying the collision of a γ particle and a proton with a production of either another γ particle, known as Compton scattering, or a π^0 particle where the π^0 decays to two photons. Through event selections and precise kinematic cuts, I am able view these two reactions respectively, but with a lot of similarities, it is hard to view either reaction by it self.

2.2 Linearly polarized photon beam asymmetries

Understanding the beam asymmetry for the reactions that this work looks at, gives the ability to extract the crucial quantum numbers (*i.e.* $\mathbf{J^{PC}}$ numbers) from the distribution produced.

Figure 2.4 is a representation of how the beam asymmetry is extracted. The polarized photon beam comes into the liquid hydrogen target in the GlueX experiment parallel to the lab floor. Once the beam collides with the protons in the target, then mesons are produced from this interaction. The ϕ angle separating the meson production plane and the polarization plane is the angle needed to compute the beam asymmetry. For the GlueX experiment, there are two orientations for the beam asymmetry: PARA (linear polarization parallel to the floor) and PERP (linear polarization perpendicular to the floor).

The cross section $d\sigma$ for the photoproduction of pseudoscalar mesons is the fol-

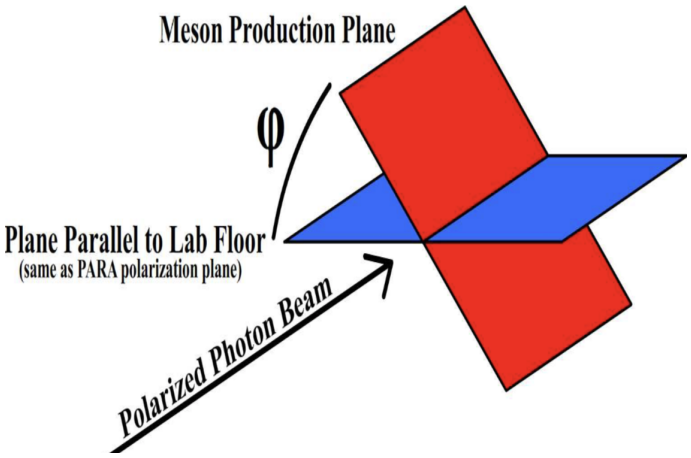

Figure 2.4: This graphic shows the angle ϕ of the beam asymmetry. Here the red plane is the meson production plane, the blue plane is the lab floor, while the beam is coming from left to right. Where the meson production plane and lab floor plane intersect is the liquid hydrogen target.

lowing:

$$d\sigma = d\sigma_0(1 - P_\gamma \Sigma cos(2\phi)) \tag{2.8}$$

Here, $d\sigma_0$ is the unpolarized cross section, ϕ is the azmuthal angle mentioned before, P_γ is the polarization of the photon, and Σ is the linearly polarized beam asymmetry. As shown, the beam asymmetry has a $\cos(2\phi)$ dependence. In order to fit this $\cos(2\phi)$ dependence to extract Σ, the need for extremely pure samples of the reactions observed are needed. This is were the challenge lies.

2.3 Monte Carlo simulations

The Monte Carlo method relies on repeated random sampling to obtain numerical results. The main idea behind this is to use randomness to solve problems that might be deterministic in principle.

An example can be done by calculating the constant π. As shown in Fig. 2.5, by drawing a circle that has the same diameter and exact domain as a square, simulated random x and y points will produce a ratio of points inside the circle and out side it.

Indeed, there are fewer points outside of the circle than inside of it. The area of this circle is simply π since the units of the square is 2 units $\times$ 2 units.

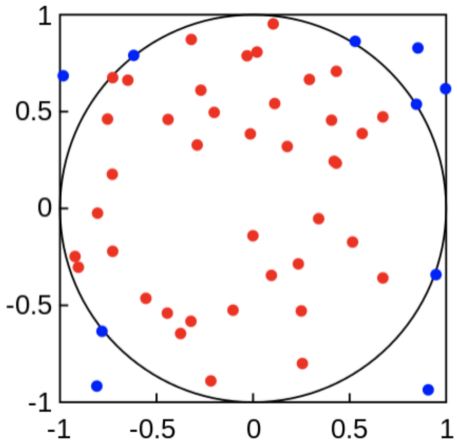

Figure 2.5: This is an example figure of the calculation of π by the Monte Carlo simulation. Points are generated randomly within the square. The ratio of the points inside of the circle and the total number of points is $\pi/4$. This is used to estimate π to almost exactness.

This example shows how Monte Carlo simulations use randomness to calculate approximate results. At Jefferson Lab, Monte Carlo simulations are conducted similarly to this one in order to produce predictions for outcomes of specific reactions that can be compared to what the actual data produces. Our Monte Carlo simulations are produced through a software called Geant3.

2.3.1 GEANT simulations

In this research project, the specific type of Monte Carlo simulations that are used are produced by a software called GEometry ANd Tracking or GEANT [9]. This software is designed to cope with many different types of experiments. The software gathers kinematic generations, tracks the particles trajectories in space, and gathers the particle's information from simulated detectors. In order to run the simulation for a specific experimental setup, GEANT requires some "description" of the media the particles are traveling through and the detector specifics.

Chapter 3

Experimental Setup

Jefferson Lab is located in Newport New, Virginia. On site, it has four experimental halls A, B, C, D; each with it's own agenda and different focus on how to explore the nature of matter. Fig. 3.1 shows a diagram of the accelerator side of JLab.

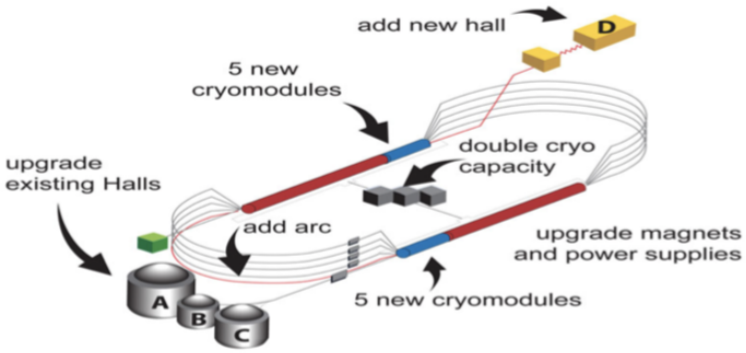

Figure 3.1: This diagram shows the electron accelerator along with the four halls of JLab. The electron races around this track picking up speed along to the straight paths. Each Hall shown can run independently from one another.

In the picture, the race track shape is the electron accelerator path. As the electron races around the track, it picks up speed on the straight portion where Radio Frequency cavities are located that accelerate the electrons. Magnets in the bend sections steer the beam around the arcs. Each hall has an independent beamline and can be provided with different beam intensities, as required.

For this honors research project, the focus is in Hall D, home of the GlueX experiment. This hall is very unique because of its large acceptance detector, is the only hall that uses a linearly polarized photon beam, and is able to reach the maximum 12 GeV energy range unlike the other halls. Below is a diagram of the GlueX detector.

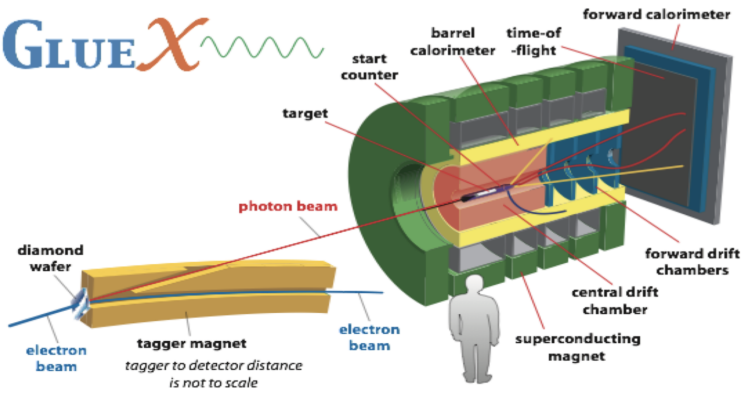

Figure 3.2: This diagram shows the GlueX detector. The beam travels from left to right. The liquid hydrogen target is shown in the very center where the Central Drift Chamber, the Barrel Calorimeter, and the super conducting solenoid magnet is surrounding it.

When the electron beam accelerates to approximately 12 GeV, it is then sent to Hall D. Note, this electron beam is a continuous beam with pulses every 4 ns. Once in Hall D, the electron hits a diamond wafer. The reason for this is because once the electron hits the diamond, Bremmstrauhlung radiation occurs and so a linearly polarized photon with the same energy is produced along with the same electron but with less momentum. The electron beam is magnetically bent away from the photon and sent to an electron dump. The linearly polarized photon will be either polarized in the parallel orientation or the perpendicular orientation as described earlier in theory section. Once produced the photon will be tagged and then sent along the beam

line where it will eventually collide with a stationary, vat of liquid hydrogen. The γp collisions happen here since the photons will be colliding with hydrogen atoms, which are just essentially protons. Surrounding the liquid hydrogen is the central drift chamber, the barrel calorimeter, as well as a super conducting magnet with approximately 2T field. These are in place in order to gather several types of data: the energy deposition of the particles produced, along with the momentum, position, and various other observables. Further down stream, the detector contains the forward drift chambers as well as the time of flight and forward calorimeter. These detectors are in place to observe the particles with smaller decay angles as well as when some particles travel further than just the barrel calorimeter. In order to view these events, GlueX reconstructs all the particle trajectories, momentum, energy depositions, etc. and stores the data in compressed files for later analysis.

Chapter 4

Results

4.1 Initial Event Selection

As stated in Chapter 2.2, in order to observe the beam asymmetry for any reaction, an extremely pure sample of the reaction must be available. I initially made simple vertex cuts, 4-momentum cuts, and energy cuts where needed.

One fix to my analysis dealt with fixing the accidentally tagged linearly polarized photons.

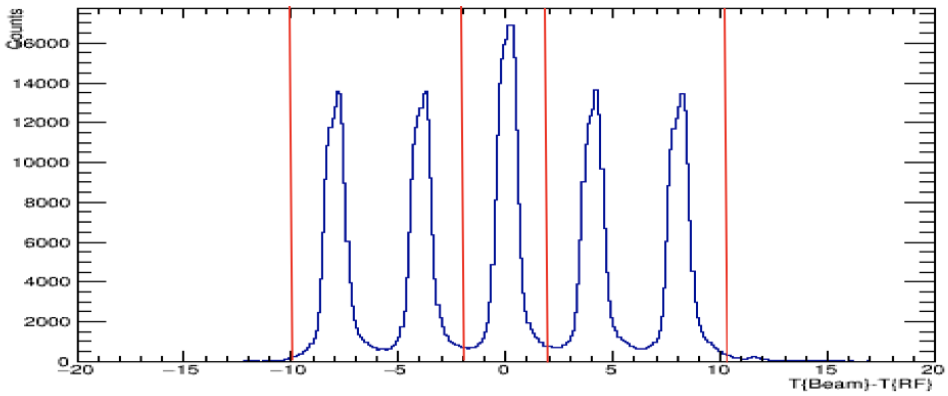

Figure 4.1: This distribution shows where there are accidentally tagged photons on the outer edges. On the x-axis is the measured time of the beam subtracted by the measured time of the radio frequency. On the y-axis is the individual counts. The actual signal is located in the center and is surrounded by the accidentally tagged photons.

As seen above in Fig. 4.1, the main signal is focused in the middle and four fake

signals are shown in the red lined region. The fake signals are where the photons were tagged incorrectly. I placed a cut to leave only the true signal in the middle as shown with the red lines.

I was able to take a quick look at the beam asymmetry at this early stage of background depletion as well. This is shown in Fig. 4.2 where the yield is plotted versus ϕ_p.

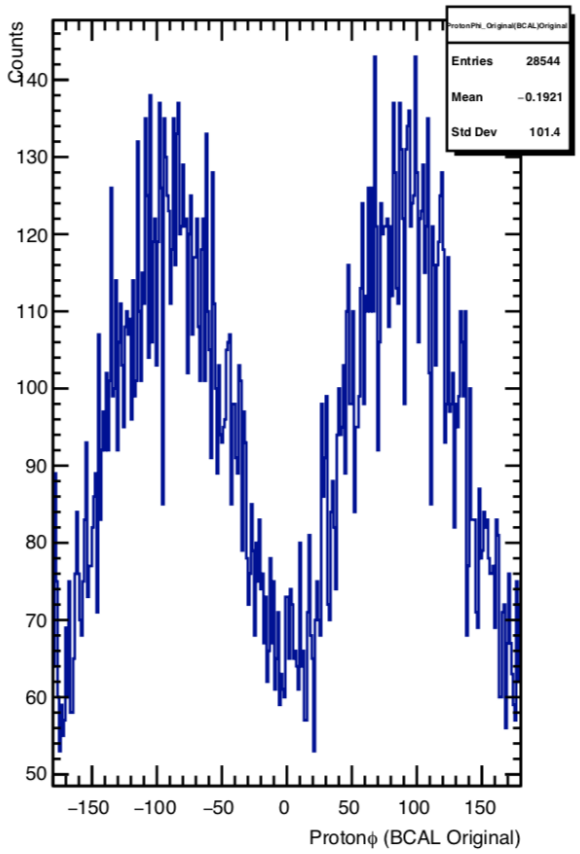

Figure 4.2: The beam asymmetry with an unpure sample. Although the distribution shows the $cos(2\phi)$ distribution I would like, there are too many uncertainties in this current sample to extract an accurate Σ beam asymmetry out.

As can be seen, there is a $cos(2\phi)$ distribution. Although the distribution can be seen and the Σ can be extracted for the beam asymmetry, there is a large uncertainty associated with it due to a limited understanding of the background contributions at

this stage of the analysis.

The next big depletion in background data came when thinking about my two reactions, $\gamma p \to \gamma p$ and $\gamma p \to \pi^0 p$, in the same manner. The data that I am looking at has both reactions inside of it, so I was observing Compton events along with π^0 events at the same time. In order to get a pure sample of Compton events, I had to get rid of all the π^0's. This is tricky since $\pi^0 \to \gamma\gamma$ around 99% of the time. By taking into consideration the $\Delta\phi$ distribution, I knew the following

$$\Delta\phi = \phi_p - \phi_\gamma \tag{4.1}$$

where ϕ_p is the ϕ angle of the proton and ϕ_γ is the ϕ angle of the γ as described in Chapter 2.

In a Compton scattering process, then the $\Delta\phi$ distribution should remain around 180°. The reason this is the case is that this process is called a "back-to-back" process where the proton and the photon separation produces a 180° angle. This is just momentum conservation. A small diagram is shown below in Fig. 4.3.

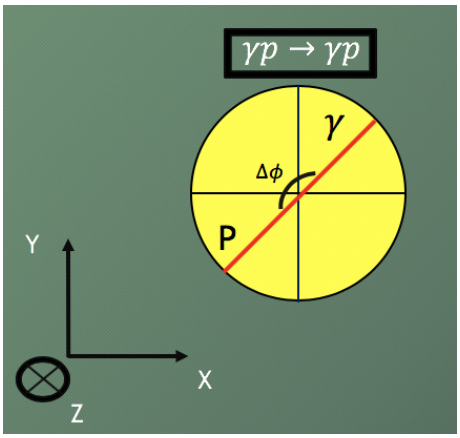

Figure 4.3: Compton scattering momentum conservation. Here is a schematic showing the phi angle being 180° in Compton scattering. The yellow circle is the BCAL with 'z' being the beam line.

In π^0 production, then the $\Delta\phi$ distribution may not be 180°. The reason this is the case is that since the π^0 decays into two photons then the proton and the photon separation does not produce a similar angle. A small diagram of the process is shown in Fig. 4.4 below.

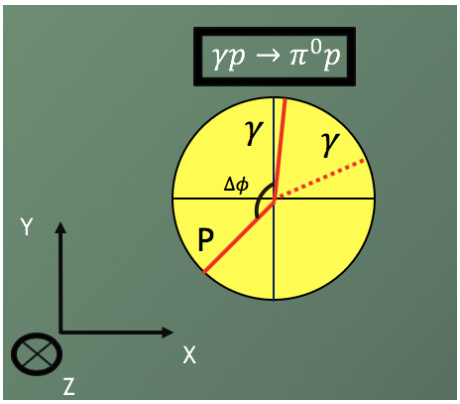

Figure 4.4: π^0 decay. Here is a schematic showing the ϕ angle of a π^0 production that would not be 180°. The dotted γ is a depicted photon that represents a photon that came from the decayed π^0 that has not been detected by the BCAL. The yellow circle is the BCAL with 'z' being the beam line.

In looking at the $\Delta\phi$ distribution along the $-t$ (the negative t channel) then I saw exactly what I expected in Fig. 4.5.

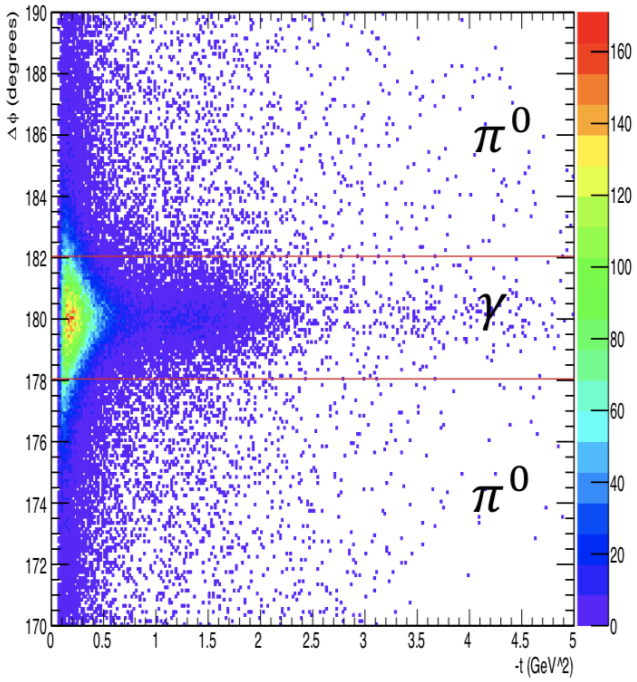

Figure 4.5: Here's the $\Delta\phi$ distribution with real data. On the x-axis is the Mandelstem variable t at low GeV^2 and on the y-axis is the $\Delta\phi$ in degrees. Outside of the main peak are a large contribution of π^0 particles while inside the main peak contains mostly γ particles. The color bar shows the amount of particles (*i.e*, purple means a small amount of particles in the area, but red means a large amount of particles in the area.) The red lines near the peak of the histogram help with visualization.

As you can see from the Fig. 4.5 histogram, the x-axis is the $-t$ channel shown in GeV^2 and the y-axis is in degrees. The 180° peak is clearly shown but the distribution has a wide base since there are π^0 particles that don't have a back-to-back process like the Compton photons have. To deplete the back ground and gain a purer sample for Compton events, I placed a cut around the 178° and 182° so as to not make too close of a cut yet. This cut is represented with the red lines on the histogram.

After placing the $\Delta\phi$ cut, I needed a way to view how well this cut took away the background, so I decided to view the $\Delta Energy$ vs. $\Delta\theta$ distribution. In this case,

$$\Delta Energy = PhotonEnergyShower - PhotonMomentum_{(missing)} \tag{4.2}$$

and

$$\Delta\theta = \theta_{measured} - \theta_{missing} \tag{4.3}$$

where the $PhotonMomentum_{(missing)}$ and $\theta_{missing}$ are what the measurements should be.

Theoretically, this distribution is supposed to be centered around (0,0), but as can be seen in Fig. 4.6. this is not the case.

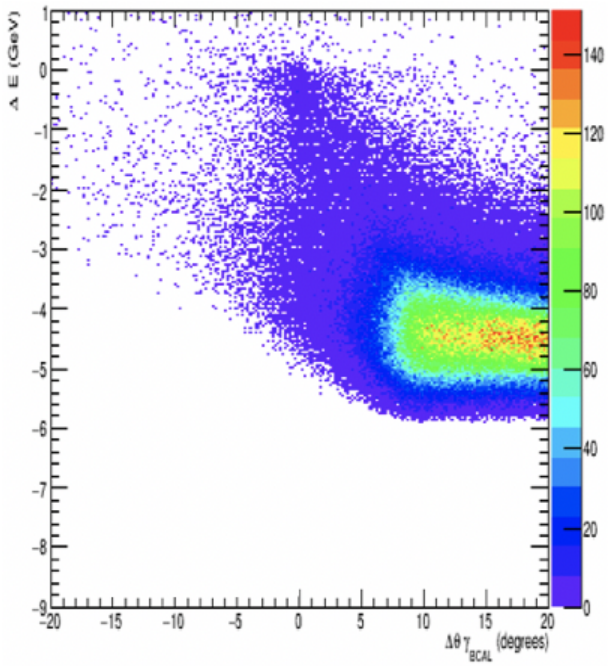

Figure 4.6: Here's the ΔE vs. $\Delta\theta$ distribution before the $\Delta\phi$ cut has been placed. This shows that something is being measured incorrectly because there is no conservation of momentum.

When placing the cut on $\Delta\phi$ as seen in the red bars in Fig. 4.5, this is when I can start seeing the data being centered at (0,0) in the histogram of ΔE vs. $\Delta\theta$ like I theorized. The only problem is that there is still a large background shown between $-6 < \Delta E < -1$ and $0 < \Delta\theta < 20$. There is some speculation as to what this background is, specifically just an incorrect $PhotonMomentum_{(missing)}$ and $\theta_{missing}$, but there's no concrete evidence to support the idea yet. So, by placing cuts at $\Delta\theta = 2$ and $\Delta\theta = -2$ as well as at $\Delta E = -4$ and $\Delta E = 4$ as can be seen in Fig. 4.7, I was able to keep the main signal that kept momentum conserved.

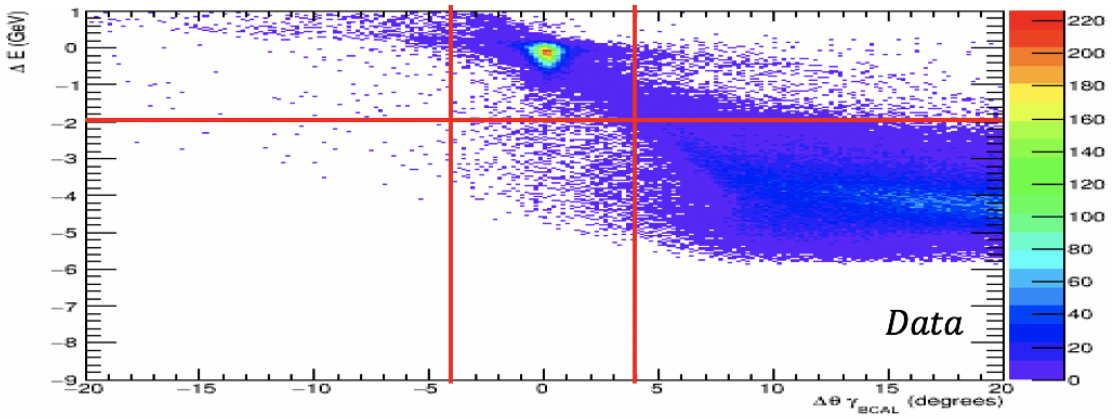

Figure 4.7: Here's the ΔE vs. $\Delta\theta$ distribution after the $\Delta\phi$ cut has been placed. This helps fix the large amount of background problem, showing that there is conservation of momentum. There is still a large amount of background noise that is thought to be incorrectly calculated values. The cuts that were placed are seen in red lines.

4.2 Shower Shape Variables

The newest portion of my work contains a solution to an old problem occurring in the GlueX's calorimeter clustering algorithm. As stated previoulsy, the π^0 decays into two photons 99% of the time. According to GlueX's current clustering algorithm, then this decay is addressed by the 1st moment. This 1st moment is defined as:

$$E_{BCAL} = \Sigma_i E_i \tag{4.4}$$

and

$$\overline{\phi}_{BCAL} = \Sigma_i E_i \phi_i \tag{4.5}$$

Eqs. 4.4 and 4.5 describe the the particles energy deposition into the detectors in the Barrel Calorimeter (BCAL). Eq. 4.4 just sums over the energies E_i deposited into each module in the BCAL and Eq. 4.5 is just the sum over the energies along the azmuthal angle ϕ_i. A diagram of two different photon showers is shown below in Fig. 4.8.

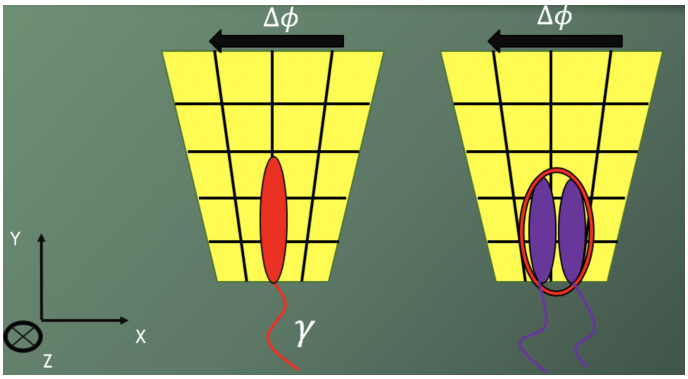

Figure 4.8: A diagram to explain the GlueX clustering algorithm. Here the azmuthal angle ϕ encircles the small sections. The squares represent individual modules of the BCAL. On the left shows a single photon shower. On the right shows the problem with the Gluex clustering algorithm when the π^0 decays into small angle photon showers.

Let's say we have a single photon shower shown on the left hand side Fig 4.8. It hits the BCAL's modules and GlueX's 1st moment clustering algorithm works fine. Now, lets say that we have a double photon shower extremely close together. This could easily be from a π^0 that had a small angle decay. Now, GlueX's 1st moment would combine these two photon showers into one big photon shower. This leaves a lot of π^0's left unaccounted for in the purification method because currently, they are being treated as just Compton events. By introducing a second moment into the picture, this small angle π^0 decay problem is fixed.

$$\sigma^2_{trans} = \sigma^2_{\phi} = \Sigma_i E_i(\phi_i - \overline{\phi})^2 \tag{4.6}$$

Here the second moment is shown in order to get a more three dimensional look at the separation of photon showers. With the second moment, there is an introduction to 3 new shower width variables shown in Fig. 4.9: $\sigma_{longitudinal}$, $\sigma_{transverse}$, σ_{θ}.

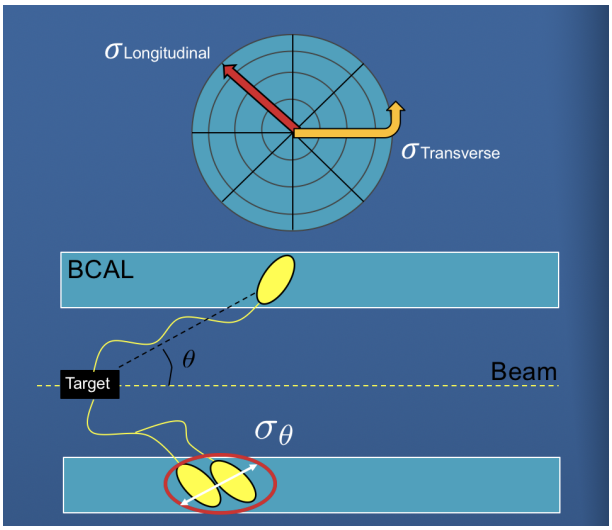

Figure 4.9: A diagram to explain the new shower width variables. The red arrow signifies $\sigma_{longitudinal}$, the energy deposition of photons. The orange arrow signifies the energy deposition along the azmuthal angle. The tricky σ_θ is shown with respect to the side of the BCAL. This variable shows the width of the photon showers from this point of view.

As shown above, the $\sigma_{longitudinal}$ variable shows the energy deposition of the photons radially outward from the target, the $\sigma_{transverse}$ shows the deposition along the azmuthal angle, and the σ_θ is shown to be the width of the photon showers when looking at the BCAL from the side. Notably, the $\sigma_{transverse}$ and the σ_θ variables will be the most important variables when looking at the separation power. The reason is that with $\sigma_{longitudinal}$ being an energy deposition variable, it is a lot harder to work with.

Looking at the purity of the shower width variables, there could be seen in $\sigma_{transverse}$ a double hump structure. It was because of this structure that this shower width variable was believed to be a great tool to observe the separation of photon showers. By looking at the Monte Carlos in comparison to the data, this showed not to be the case. By looking at Fig. 4.10 were the red is the data, the yellow is the extremely small Compton events, and the green is the π^0 events, it is seen that both

Monte Carlos favor the smaller values of $\sigma_{transverse}$.

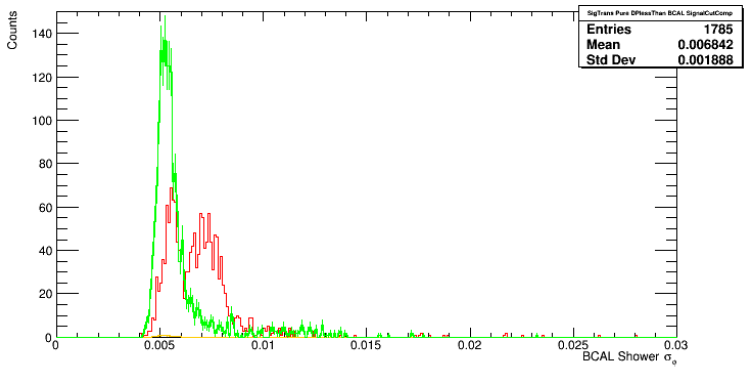

Figure 4.10: On the x-axis is the $\sigma_{transverse}$ shower values and on the y-axis are the individual counts. Here, the red is the data, yellow is the extremely small Compton events, and the green is the π^0 events. This histogram has correct scaling of Compton and π^0 events based off of a likelihood fit.

This could mean one to two things: either the Monte Carlos are incorrect or there are crucial cuts that are missing making the second hump background data. Instead of going in and trying to fix the Monte Carlos, I began to go over other possibilities that could possibly reduce the events in this histogram. Thinking about the how the BCAL takes in data, the following was observed.

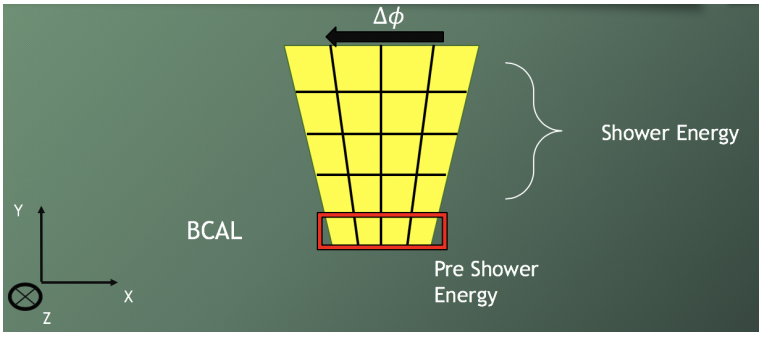

Figure 4.11: Here a wedge of the BCAL is shown. Boxed in red is known as the pre-shower energy section. The rest of the cells are known as the shower energy section.

In Fig. 4.11, when a photon shower hits the BCAL, each individual cell will gather the energy that was deposited in them. When the energy is deposited in the red box then it is known as the pre-shower energy, and outside of the box it is known as the shower energy. By plotting $\sigma_{transverse}$ vs. the pre-shower energy (similar results can be seen with σ_θ) it can be seen that there is background in the top left hand corner as shown in Fig. 4.12.

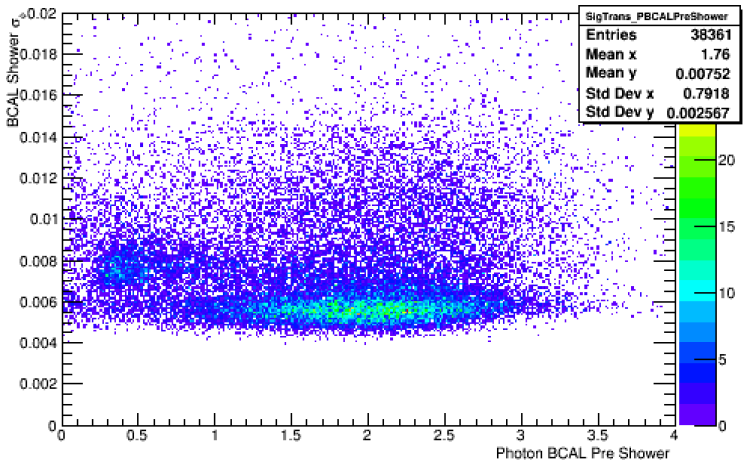

Figure 4.12: Here is the plot of $\sigma_{transverse}$ vs. Photon BCAL PreShower Energy where $\sigma_{transverse}$ is on the y-axis and Photon BCAL PreShower Energy is on the x-axis. The background in the histogram less than 1 was cut in order to observe the depletion of the background in the $\sigma_{transverse}$ shower width variable.

Essentially, the main signal is when the photon showers are wider while the small signal in the left hand corner is when the photon showers are slimmer. Since I wanted to look at the wider photon showers, I placed a cut at one in order to look at mainly wider photon shower widths.

Now looking at the ratio of the pre-shower energy and the shower energy along with the $\gamma\theta$-determined (photon theta), it can be seen in Fig. 4.13 that a cut needs to be placed on the ratio along 0.4. To describe $\gamma\theta$-determined in more depth, we know that $\gamma\theta$ is the physical polar angle of the photon from vertex when the particle is produced in the target. So, $\gamma\theta$-determined is $\gamma\theta$ but with a hard cutoff at the end of

the BCAL and makes sure that nothing is smeared out by the collisions that occur in the target. Applying this allows me to look at any edge effects that may be present.

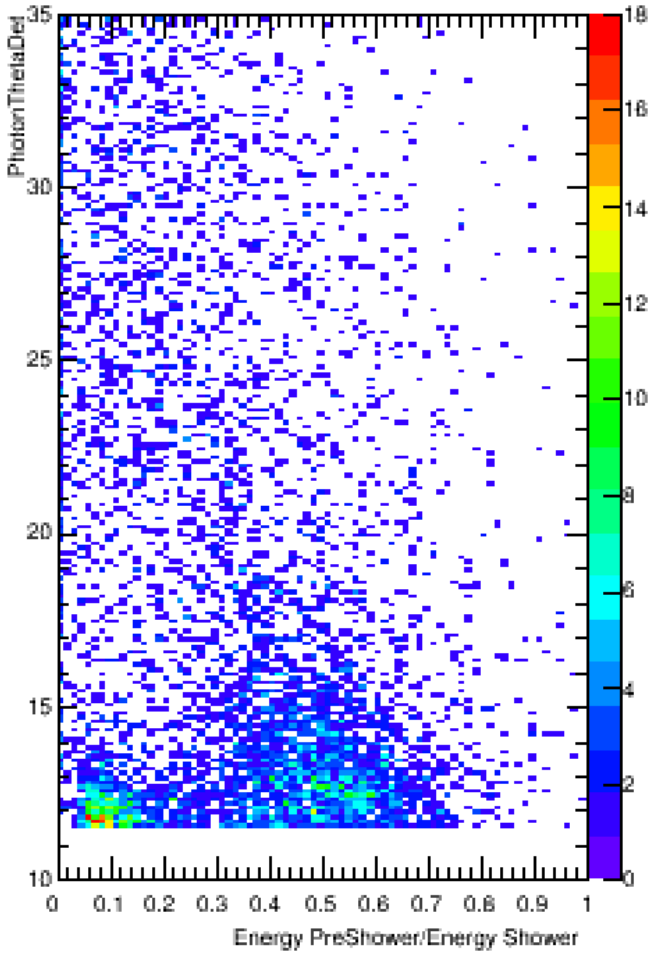

Figure 4.13: Here is the plot of the $\gamma\theta Det$ vs. PreShower Energy/ Shower energy ratio where $\gamma\theta Det$ is on the y-axis and PreShower Energy/ Shower energy ratio is on the x-axis. The background in the histogram is less than 0.4 on the ratio and a cut was made in order to observe the depletion of the background in the $\sigma_{transverse}$ shower width variable.

I placed a cut at the ratio of 0.4 and not around 0.2 where the majority of the background signal is simply because to me, the background seemed to have a tail that crossed into actual signal. I wanted to make sure that I depleted all the background right away knowing later I would go back and optimize that cut I placed.

After this depletion, I then looked at the $\sigma_{transverse}$ variable to see if the cuts that were now applied reduced the events any. In Fig. 4.14, it can be see that the cuts reduced the second hump significantly and so it is observed now that the $\sigma_{transverse}$ shower width variable is not a good separating variable based off of the hypothesis made before.

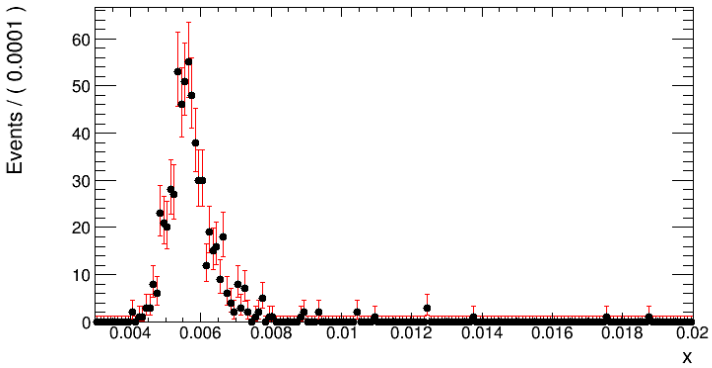

Figure 4.14: On the x-axis is the $\sigma_{transverse}$ shower values and on the y-axis are the individual counts. Notice the large reduction in the second hump to the right from before.

4.3 Likelihood Fits

The next idea was to see how many π^0 events the reaction had left in the current data. After generating new date Monte Carlo simulations with each of these new variables included, a likelihood event was taken of each of the variables independently and then together in two dimensions.

A likelihood is the value of a probability density function evaluated at the measurable value of the observable. Essentially what a likelihood fit does is estimates model

parameters from the Monte Carlo simulations and assigns the a weight such that when you apply the weight and sum the Monte Carlo results together, you get what the original data distribution looks like. It finds the maximum agreement between the Monte Carlos and the actual data In mathematical terms, we use

$$f(\sigma_i) = w_{\pi^0} \cdot f_{\pi^0 MC}(\sigma_i) + w_\gamma \cdot f_{\gamma MC}(\sigma_i) \tag{4.7}$$

In Eq. 4.7, $f(\sigma_i)$ is the function of σ_i where σ_i is obtained by summing the π^0 and Compton functions multiplied their respected weights calculated from the estimated parameters. Also, $f_{\pi^0 MC}(\sigma_i)$ and $f_{\gamma MC}(\sigma_i)$ are the functions of σ_i the respected Monte Carlos and w_{π^0} and w_γ are the weights computed of the respected particle distributions. In general, this is just trying to find by what scaling factor I can apply to the π^0 and Compton Monte Carlos in order to get the distribution given with actual data.

The following plots of Fig. 4.15, 4.16, and 4.17 show the fits applied to the distributions of each individual σ variables.

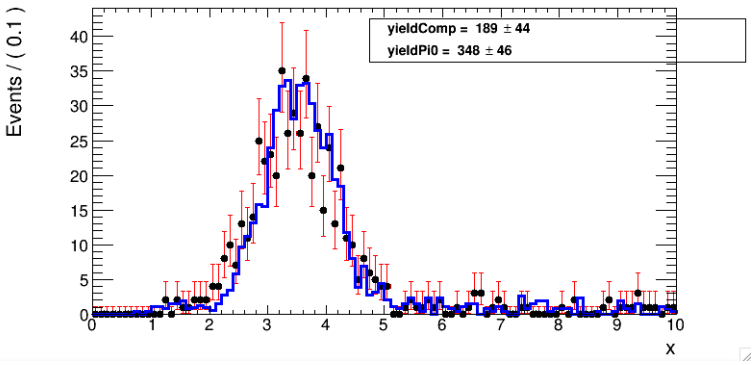

Figure 4.15: The fit of the $\sigma_{longitudinal}$ shower width variable. On the x-axis is the $\sigma_{longitudinal}$ shower values and on the y-axis are the individual counts. The red is the actual data while the blue is the likelihood fit. As seen, the fit does not match the data because all the way since this is an energy deposition shower variable. Since π^0 may decay into low energy photons, this variable is not reliable.

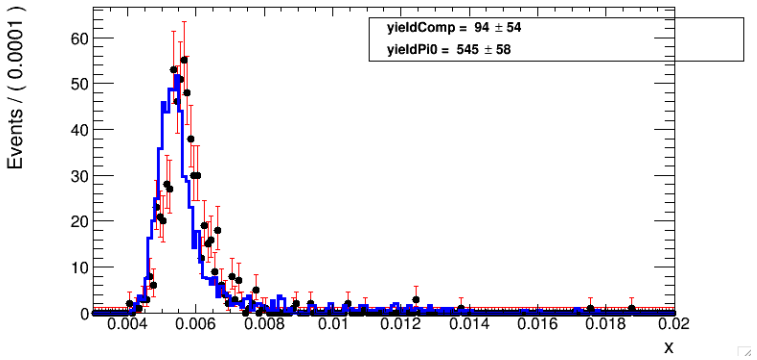

Figure 4.16: The fit of the $\sigma_{transverse}$ shower width variable. On the x-axis is the $\sigma_{transverse}$ shower values and on the y-axis are the individual counts. The red is the actual data while the blue is the likelihood fit.

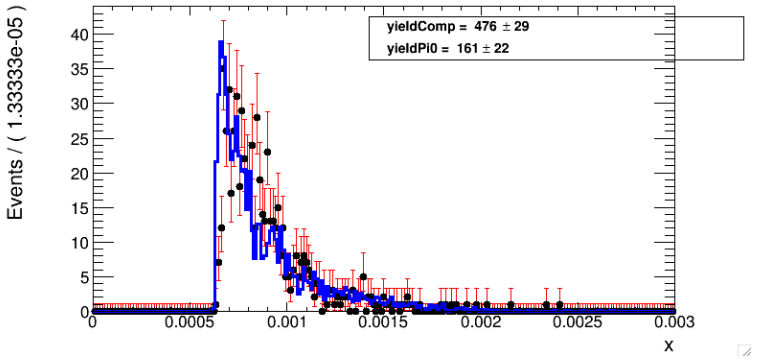

Figure 4.17: The fit of the σ_θ shower width variable. On the x-axis is the σ_θ shower values and on the y-axis are the individual counts. The red is the actual data while the blue is the likelihood fit.

In these histograms, the red and black dots are the data points of the σ variables and the blue is a RooFit (a fitting algorithm that can fit Probability Distribution Functions) that is applied in order to obtain the weights from each variable as addressed earlier. The separation power can not be seen in the any of these shower width variables from the likelihood fit. By looking at the data versus the Monte Carlos scaled with the correct values gathered from the likelihood fits, I can see that the best view of the separation power is in σ_θ shown in Fig. 4.20.

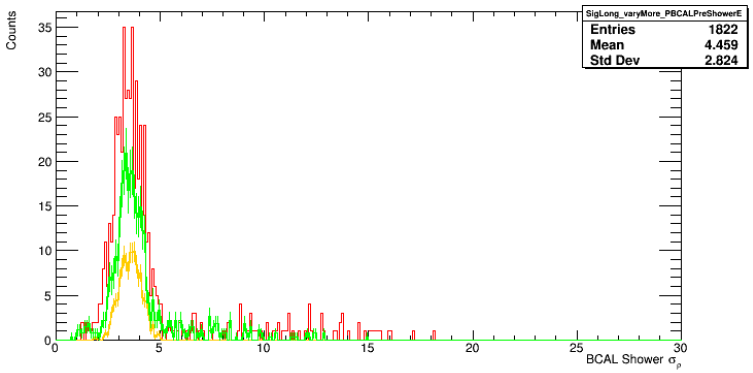

Figure 4.18: The fit of the $\sigma_{longitudinal}$ shower width variable. On the x-axis is the $\sigma_{longitudinal}$ shower values and on the y-axis are the individual counts. The red is the actual data while the yellow is the Compton Monte Carlo and the green is the π^0 Monte Carlo. Since both Monte Carlos align on top of each other, there is no way to separate the events with this variable.

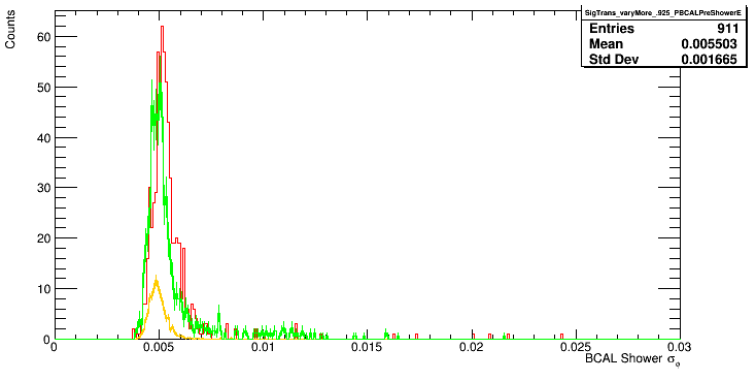

Figure 4.19: The fit of the $\sigma_{transverse}$ shower width variable. On the x-axis is the $\sigma_{transverse}$ shower values and on the y-axis are the individual counts. The red is the actual data while the yellow is the Compton Monte Carlo and the green is the π^0 Monte Carlo. Since both Monte Carlos align on top of each other, there is no way to separate the events with this variable.

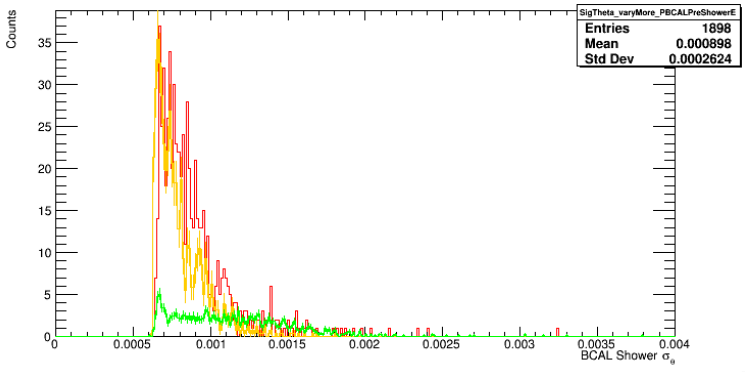

Figure 4.20: The fit of the σ_θ shower width variable. On the x-axis is the σ_θ shower values and on the y-axis are the individual counts. The red is the actual data while the yellow is the Compton Monte Carlo and the green is the π^0 Monte Carlo. As seen there is a big difference between the two Monte Carlos.

To describe the σ_θ histogram in depth, the yellow Compton signal should only have a narrow peek because there should only be one observed single photon shower. The green π^0 signal also has a small narrow peek at low σ_θ because sometimes the π^0 decays into different range of energy sizes. If the π^0 decays into one photon shower with 10 GeV and one photon shower with 1 GeV, then the 1 GeV photon will not be observed inside the BCAL since the giant magnet will bend it out. So, this is what is happening with the small narrow peek. The broad hump is the opposite of this when two photon showers are observed leaving a larger range in σ_θ.

4.4 Scaling Factors for Data and Monte Carlo Agreement

Noticing that the likelihood fit's were slightly askew from data distribution, meaning that the Monte Carlo's were off a bit from data, I placed multiple unbiased scaling factors to the data. The reason I scaled the data instead of scaling the Monte Carlo's is because going in and changing the Monte Carlo's would take months, so scaling the data is less time consuming. I took the χ^2 of the scaling factors and the likelihood fits to determine which scaling factor would be best for the data. By plotting the scaling factors vs the computed χ^2 it can be seen that there is a single point for both histograms of $\sigma_{transverse}$ and σ_θ where the χ^2 is at a minimum.

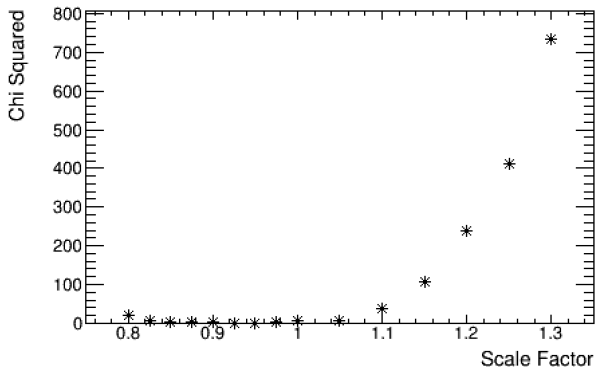

Figure 4.21: The plot of the χ^2 values of the scaling factors and the likelihood fits vs the scaling factors of the data. As can be seen, there is a minimum χ^2 value near the center of the parabolic looking distribution.

As seen in Fig. 4.21, the distribution has a parabolic look to it where the values tend to the smallest χ^2 value and then shoot off to infinity the further away you get from that value. This is because the further you move the data from where the Monte Carlo's are situated, the worse the χ^2 value will be. Closing in on the smaller χ^2 values, I can see this parabolic distribution better with the smallest χ^2 value at the bottom in Fig. 4.22. I have placed a polynomial fit on the data to show the parabola better.

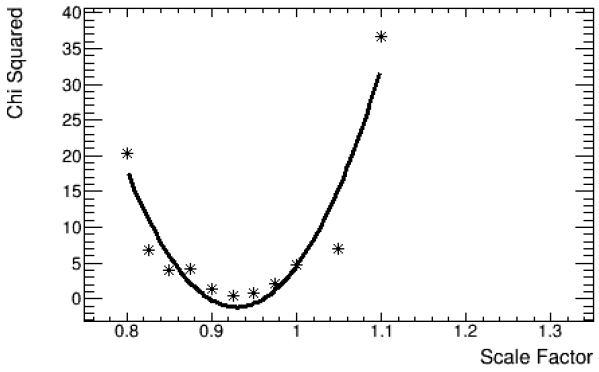

Figure 4.22: The plot of the χ^2 values of the scaling factors and the likelihood fits vs the scaling factors of the data with the smaller χ^2 values plotted. As can be seen, there is a minimum χ^2 value near the center of the parabola.

Looking at σ_θ is slightly different. Varying the data for σ_θ affects the Probability Density Function of the data in the algorithm that I use to create the likelihood fit. In changing this, then the likelihood fit, as the data is moved towards the right, changes into a more broader function that seems to correlate with the broadness of the data distribution, but I know that this is incorrect. So, greater than a scaling factor of one will not be correct.

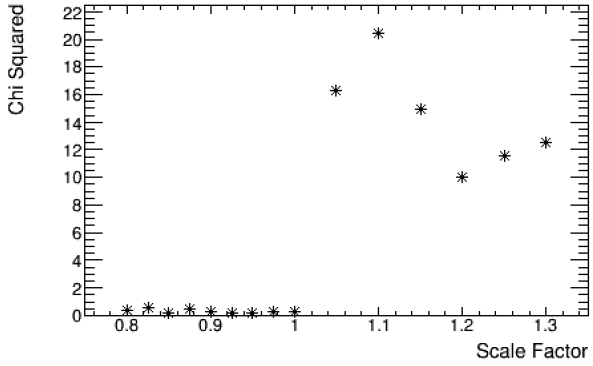

Figure 4.23: The plot of the χ^2 values of the scaling factors and the likelihood fits vs the scaling factors of the data. As can be seen, the right hand side of the distribution looks scattered and does to go to infinity the further out the I go from the histogram. This is essentially due to the specifics of algorithm that I use to calculate the likelihood fits.

As it can be seen by looking at Fig. 4.24, the likelihood fit has been affected

allowing for smaller χ^2 values to be obtained. Now focusing on the smaller χ^2 values, a similar thing can be seen.

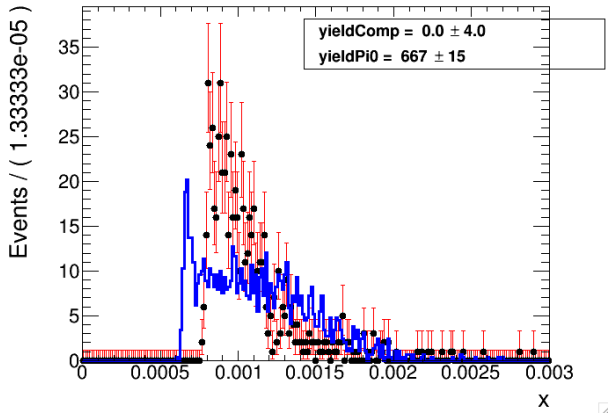

Figure 4.24: This is the histogram of σ_θ in red and the likelihood fit in blue with a scaling factor of 1.15 and a χ^2 value of 14.8255. As can be seen, the likelihood fit has shrunk compared to the original plots shown earlier.

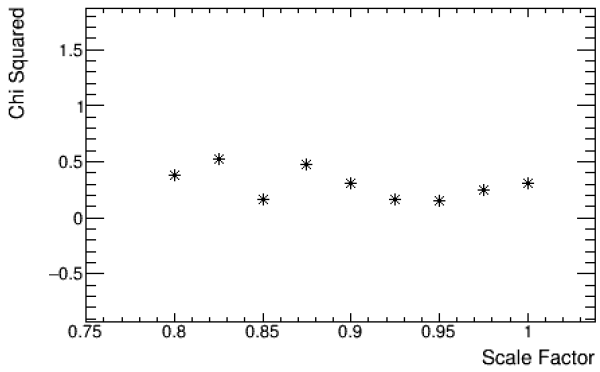

Figure 4.25: The plot of the χ^2 values of the scaling factors and the likelihood fits vs the scaling factors of the data with the smaller χ^2 values plotted. As can be seen, the left hand side of the distribution looks scattered. This is essentially due to the broadness of the σ_θ distribution. By varying the data in this range this produced smaller χ^2 values even though the data was not perfectly aligned as I wanted.

This problem on the left hand side of Fig. 4.25 is essentially due to the broadness of the σ_θ distribution allowing for smaller χ^2 values to be calculated even though the data was not perfectly aligned. This can be seen in an example outlier on Fig. 4.26

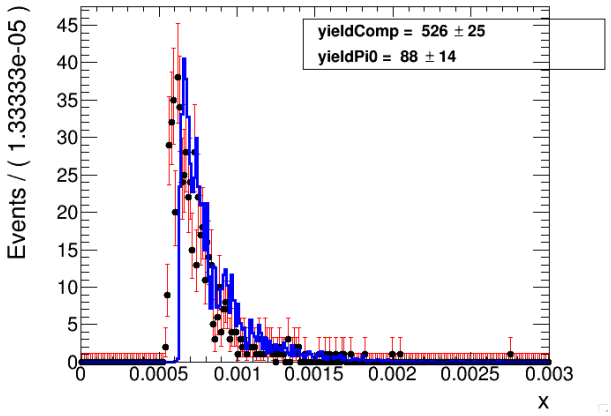

Figure 4.26: This is the histogram of σ_θ in red and the likelihood fit in blue with a scaling factor of 0.85 and a χ^2 value of 1.6856. As can be seen, the broadness of the distribution will affect the χ^2 value.

By not focusing on such a broad range of scaling factors as to not incorporate these problems, I can see the parabolic distribution arise as with $\sigma_{transverse}$ in the range of 0.9 to 1.0.

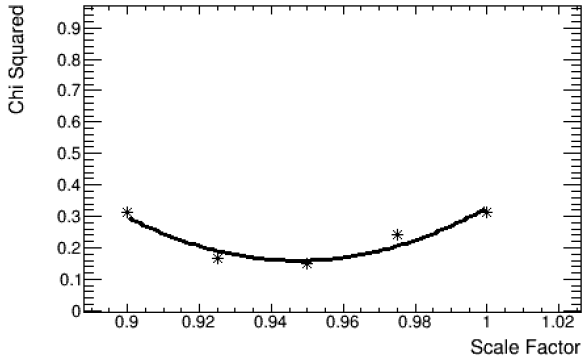

Figure 4.27: The plot of the χ^2 values of the scaling factors and the likelihood fits vs the scaling factors of the data with the smaller χ^2 values plotted. As can be seen, there is a minimum χ^2 value near the center of the parabola.

Figures 4.28 and 4.27 show the histogram where the smallest χ^2 value was determined out of the scaling factors. The scaling factors that I applied were: 0.925 for $\sigma_{transverse}$ (with a χ^2 value of 0.47022) and 0.95 for σ_θ (with a χ^2 value 1.49115 .

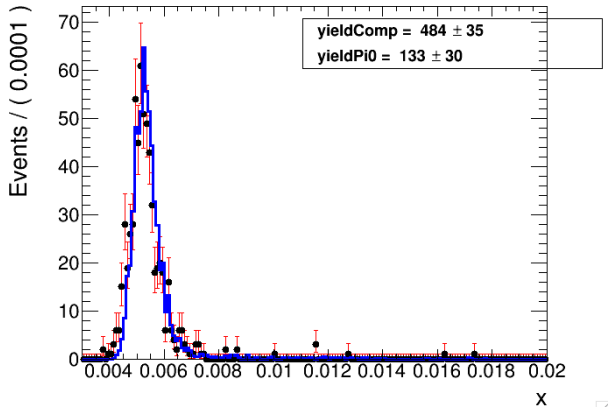

Figure 4.28: The fit of the $\sigma_{transverse}$ shower width variable with a scaling factor of 0.925. On the x-axis is the $\sigma_{transverse}$ shower values and on the y-axis are the individual counts. The red is the actual data while the blue is the likelihood fit. As it can be seen, the total number of Compton events rose tremendously.

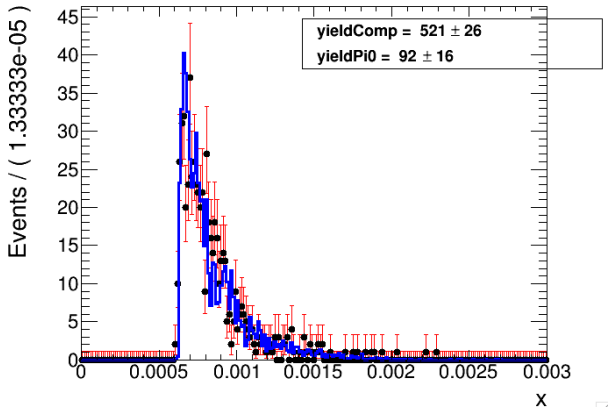

Figure 4.29: The fit of the σ_θ shower width variable with a scaling factor of 0.95. On the x-axis is the σ_θ shower values and on the y-axis are the individual counts. The red is the actual data while the blue is the likelihood fit. As it can be seen, the total number of Compton events rose as well.

As it can be seen, the likelihood fits accurately describe the data unlike Figures 4.16 and 4.17 before. In doing this, the algorithm I used for the likelihood fit is able to determine, with better precision, how many Compton events versus π^0 events there are in the data now. Where before there was a minuscule amount of Compton events contained in the $\sigma_{transverse}$, it can be seen that there are much more currently in the updated version. This can also been seen in looking at the Monte Carlos versus the data.

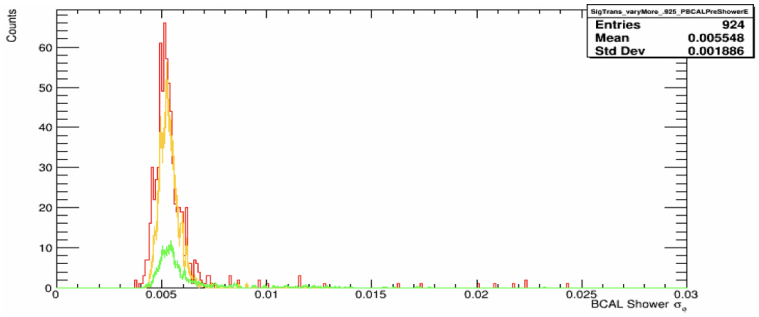

Figure 4.30: The fit of the $\sigma_{transverse}$ shower width variable. On the x-axis is the $\sigma_{transverse}$ shower values and on the y-axis are the individual counts. The red is the actual data while the yellow is the Compton Monte Carlo and the green is the π^0 Monte Carlo. It is seen that the Compton and π^0 Monte Carlos switch as the updated scaling factors are applied.

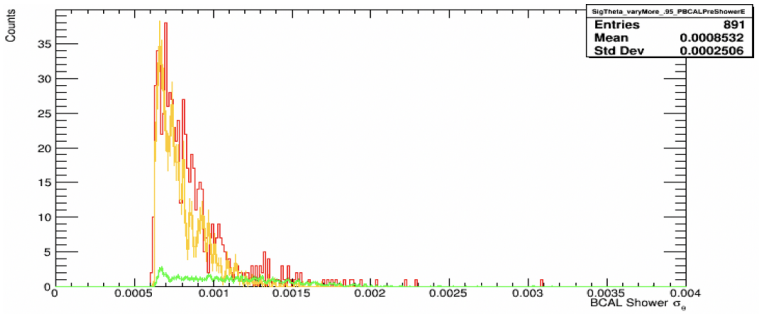

Figure 4.31: The fit of the σ_θ shower width variable. On the x-axis is the σ_θ shower values and on the y-axis are the individual counts. The red is the actual data while the yellow is the Compton Monte Carlo and the green is the π^0 Monte Carlo. It is seen that there is still a separation attribute due to the Monte Carlos.

4.5 Purity and Efficiency

Now that all the cuts had been placed, I wanted to see the purity and efficiency of the best separation variable I observed, the σ_θ shower width variable. By looking at both the purity and efficiency of this shower width variable, I would be able to determine the best place to separate the rest of the π^0 events from the Compton events based off of the Monte Carlos. By definition, the purity is just how pure the reaction is. In this case, I am looking at the purity of the Compton reaction specifically. To calculate this I simply compute:

$$Purity = \frac{\int_0^{\sigma_\theta^{Max}} Compton_{MC}}{\int_0^{\sigma_\theta^{Max}} Compton_{MC} + \int_0^{\sigma_\theta^{Max}} \pi^0_{MC}} \leq 1 \tag{4.8}$$

where σ_θ^{Max} is the maximum value of the bin through out each point on the x-axis, and $Compton_{MC}$ and π^0_{MC} are the Compton and π^0 Monte Carlos respectively. To explain this in more depth, the purity starting at zero is at a maximum 1. As I increment through the values on the x-axis the purity starts exponentially decrease until it reaches the end of the data. This exactly what I observe.

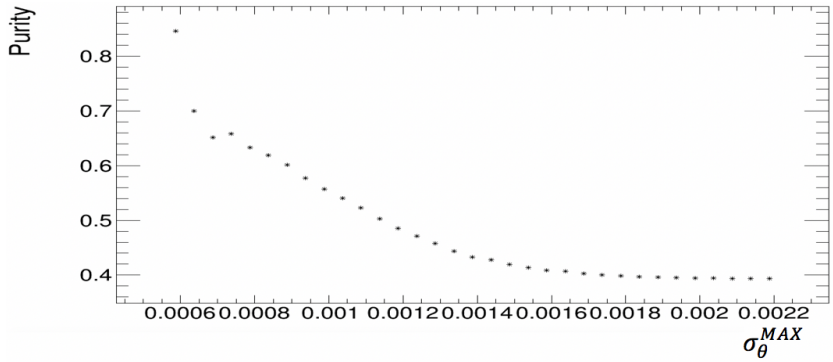

Figure 4.32: A graph of the purity of Compton events in the data. On the x-axis is the maximum value of the bin while the y-axis contains the actual purity vlaue. The distribution has an exponential decay as expected.

By definition as well, the efficiency is just how much events that have been cut. In this case, I am looking at the efficiency of the Compton reaction specifically. To calculate this I simply compute:

$$Efficiency = \frac{\int_0^{\sigma_\theta^{Max}} Compton_{MC}}{\int_0^{\infty} Compton_{MC}} \leq 1 \tag{4.9}$$

where σ_θ^{Max} is the maximum value of the bin through out each point on the x-axis, $Compton_{MC}$ and π^0_{MC} are the Compton and π^0 Monte Carlos respectively. To explain this in depth, from there are no Compton events to get rid of at the start while looping through the data, so the efficiency values stays at zero. Then, once the loop starts to add more Compton events then the efficiency raises while maxing out at around 0.8. This is also exactly what I observe.

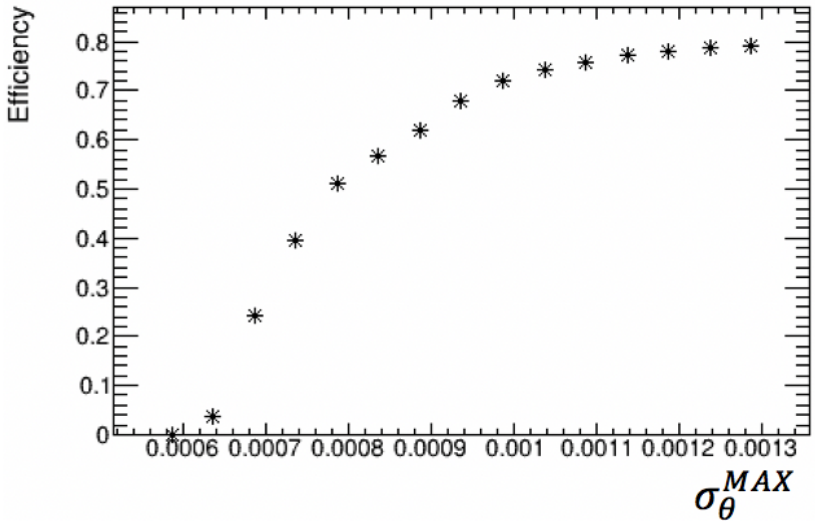

Figure 4.33: A graph of the efficiency of Compton events in the data. On the x-axis is the maximum value of the bin while the y-axis contains the actual efficiency value. The distribution drops after getting rid of Compton events as expected.

For an analysis like this, finding the best optimized value of the purity versus efficiency of Compton events is a challenging feat. In Fig. 4.34, both purity and

efficiency are plotted. It is understood that most might think the best optimization is located where the two distributions cross, but for this analysis that may not be the case. On one hand, it is best if we have a very pure sample of our Compton reaction to obtain the quantum numbers, but if the efficiency is too low and we lose too many Compton events in making the sample extremely pure, there would not be enough events left to obtain the beam asymmetry. Similarly, if we have too high of an efficiency then our sample would not be pure enough and we would have too many π^0 events in the data. So in this case, the best approach is to see where the best efficiency vs purity ratio is while keeping just enough Compton events to extract the Σ beam asymmetry.

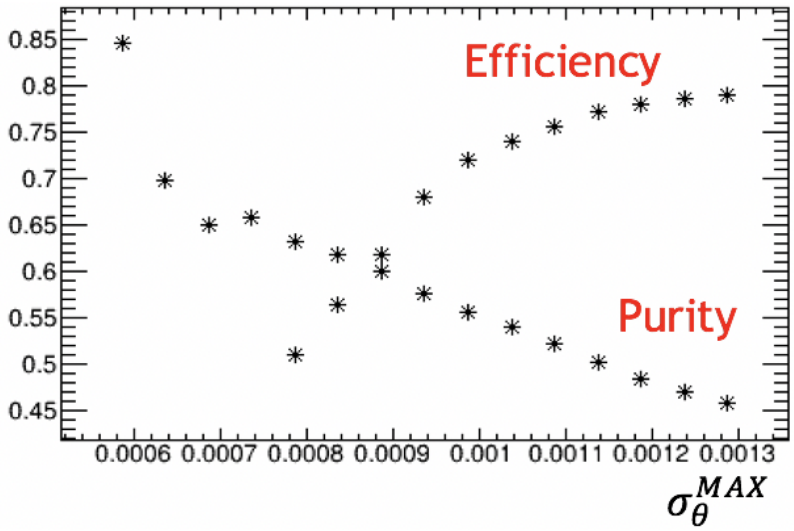

Figure 4.34: A graph of the efficiency and purity of Compton events. On the x-axis is the maximum value of the bin while the y-axis contains the actual efficiency values and purity values. The distribution going from 0.85 and dropping to 0.4 is the purity of Compton events while the distribution going from 0 to 0.8 is the efficiency of Compton events.

Chapter 5

Conclusion/Outlook

In conclusion, many milestones have been completed. Significant background reduction in both reactions have been made,and a rudimentary beam asymmetry has been extracted that has the theoretically predicted distribution. Furthermore, this work has introduced three shower width variables that have helped model the π^0 decay better.

By looking at pure samples of the shower width variables, a likelihood fit was used to determine how many Compton events versus π^0 events were in the data. With much more Compton events located in the data than π^0 events, it is noted that the back ground reduction process has been very successful. While I was hopeful that all three shower width variables would be beneficial in separating the final events, this work shows that only σ_θ will be valuable.

5.1 Future Work

Once an optimal cut has been chosen for the σ_θ shower width variable, then the next route would be to go back and look for the most optimal cuts on the other variables as well (*i.e.* $\Delta\phi$, ΔE, etc.). Once this is complete, the σ variables would need another rerun of the likelihood fits to tell how many Compton events verses π^0 events are in the data based off of the Monte Carlo simulations. If the π^0 events were

low enough, then the Σ beam asymmetry could be extracted and trusted. If not, then more background reduction would be needed.

After this part of the analysis is complete, then the work could begin to focus on looking to see if the Compton scattering process has the potential for constraining Generalized Parton Distributions.

Chapter 6

References

[1] H. Al Ghoul et al. [GlueX Collaboration], "Measurement of the beam asymmetry Sigma for pi-zero and eta photoproduction on the proton at E-gamma = 9 GeV," Phys. Rev. C 95, no. 4, 042201 (2017)

[2] T. D. Beattie et al.,"Construction and Performance of the Barrel Electromagnetic Calorimeter for the GlueX Experiment," Retrieved 14:40, November 20, 2018, from https://doi.org/10.1016/j.nima.2018.04.006

[3] Meyers, Curtis. Light and Exotic Mesons. www.curtismeyer.com/material/lecture.pdf.

[4] Donnelly T. W. Foundations of Nuclear and Particle Physics Cambridge University Press, 2017.

[5] Wikipedia contributors. "Mandelstam variables." Wikipedia, The Free Encyclopedia. Wikipedia, The Free Encyclopedia, 4 Dec. 2018. Web. 12 Apr. 2019.

[6] Wikipedia contributors. "Monte Carlo integration." Wikipedia, The Free Encyclopedia. Wikipedia, The Free Encyclopedia, 1 Mar. 2019. Web. 12 Apr. 2019. [7] Rosner, and Jonathan L. "The Eightfold Way." ArXiv.org, 15 Oct. 2001, arxiv.org/abs/hep-ph/0109241.

[8] Wikipedia contributors. "Meson." Wikipedia, The Free Encyclopedia. Wikipedia, The Free Encyclopedia, 28 Mar. 2019. Web. 12 Apr. 2019.

[9] Brun, R., et al. Geant, Simulation Program for Particle Physics Experiments; User Guide and Reference Manual. CERN. Data Handling Division, 1978.

6.1 Appendex

6.1.1 Code

https://github.com/zabaldwin